PCCP

PAPER

View Article Online
View Journal | View Issue

Cite this: *Phys. Chem. Chem. Phys.*, 2022, **24**, 14993

Electronic structure and interfacial features of triphenylamine- and phenothiazine-based hole transport materials for methylammonium lead iodide perovskite solar cells†

Carmen Coppola,[ab] Adriana Pecoraro,[c] Ana B. Muñoz-García,[c] Rossella Infantino,[de] Alessio Dessì,[e] Gianna Reginato,[e] Riccardo Basosi,[abe] Adalgisa Sinicropi *[abe] and Michele Pavone *[f]

Recently, great research efforts have been devoted to perovskite solar cells (PSCs) leading to sunlight-to-power conversion efficiencies above 25%. However, several barriers still hinder the full deployment of these devices. Critical issues are related to PCE stability and device lifetimes, which could be improved by targeted engineering of the hole transport material (HTM). Indeed, the HTM is not only responsible for transporting holes and preventing direct contact between the photo-active perovskite and the charge collector layer, but it plays important structural and protective roles too. As alternatives to the widely used yet expensive and unstable **Spiro-OMeTAD**, organic HTMs based on triphenylamine (TPA) and phenothiazine (PTZ) moieties have been proposed. However, their performances in PSC devices, and in particular their interfacial properties with the most popular methylammonium lead iodide perovskite (MAPI) still need investigations to be fully determined. In this framework, here we report a first-principles study on the structural and the electronic properties of a recently designed TPA and PTZ-based HTM (**HTM1**) and its interface with the MAPI (001) surface, considering both the PbI_2- and the MAI-terminations. We also addressed already known HTM molecular systems to allow for a direct comparison with the recently proposed **HTM1**: we characterized the molecular parameters and the MAPI/HTM interfacial properties for **Spiro-OMeTAD**, **PTZ1**, and **PTZ2**. Our results suggest that good adhesion properties do not ensure effective and efficient MAPI-HTM hole injection. Despite the theoretical good alignment between **HTM1** HOMO and MAPI valence band edge, our results for the mutually polarized interface point out the lack of a sufficient driving force for hole transport. While the hole mobility of **HTM1** outperforms those of the other HTM molecules, for this HTM molecule, our findings suggest the application of lead halide perovskite compositions other than MAPI, with substituents that lower its valence band maximum potential value.

Received 16th March 2022,
Accepted 23rd May 2022

DOI: 10.1039/d2cp01270g

rsc.li/pccp

Introduction

The photovoltaic community is devoting unprecedented efforts to perovskite solar cells (PSCs), which have rapidly increased their sunlight-to-power conversion efficiency (PCE) from 3.8% in 2009 to 25.5% in 2021.[1,2] The prototypical organic–inorganic lead halide-based perovskite is $CH_3NH_3PbI_3$, commonly known as MAPI, which possesses a direct band gap, strong absorption and good ambipolar charge carrier mobility, all factors enhancing the PCE.[3] The working principle of a PSC starts from the photoexcitation of the perovskite material, which leads to the formation of electron–hole pairs. The electrons are then injected into the electron transport material (ETM), while the holes are injected into the hole transport material (HTM), which are in contact with the transparent conductive oxide

[a] *Dipartimento di Biotecnologie, Chimica e Farmacia, R²ES Lab, Università degli Studi di Siena, via Aldo Moro 2, 53100, Siena, Italy. E-mail: adalgisa.sinicropi@unisi.it*
[b] *CSGI, Consorzio per lo Sviluppo dei Sistemi a Grande Interfase, via della Lastruccia 3, 50019, Sesto Fiorentino, Italy*
[c] *Dipartimento di Fisica "Ettore Pancini", Università degli Studi di Napoli Federico II, Comp. Univ. Monte Sant'Angelo, Via Cintia 21, 80126, Napoli, Italy*
[d] *Dipartimento di Biotecnologie, Chimica e Farmacia, Università degli Studi di Siena, via Aldo Moro 2, 53100, Siena, Italy*
[e] *Istituto di Chimica dei Composti OrganoMetallici (ICCOM), Consiglio Nazionale delle Ricerche (CNR), Via Madonna del Piano 10, 50019, Sesto Fiorentino, Italy*
[f] *Dipartimento di Scienze Chimiche, Università degli Studi di Napoli Federico II, Comp. Univ. Monte Sant'Angelo, Via Cintia 21, 80126, Napoli, Italy. E-mail: michele.pavone@unina.it*

† Electronic supplementary information (ESI) available. See DOI: https://doi.org/10.1039/d2cp01270g

(TCO) and with the metal electrode, respectively, in the normal (n–i–p) device configuration.[4,5] PSC components can also be arranged in an inverted (p–i–n) device configuration, which can guarantee higher intrinsic stability.[6] The lack of long-term stability is actually the main issue that is hampering large-scale PSC production and it can be mainly ascribed to the degradation of PSC components. In particular, it has been proven that PSC stability largely depends on the HTMs because they are responsible for the charge extraction and transfer at the interfaces while blocking charge recombination, and also act as physical barriers by preventing the contact of the active perovskite layer with the metal electrode and by blocking moisture and oxygen penetration.[7] For these reasons, the development of more efficient HTMs and the optimization of their interface with the perovskite material are the key steps in the further development of PSC devices.[8] **Spiro-OMeTAD** (2,2′,7,7′-tetrakis[*N*,*N*-di(4-methoxyphenyl)amino]-9,9′-spirobifluorene) is hitherto the most popularly employed HTM in n–i–p devices. Its energy levels are well aligned with the valence band maximum (VBM) and conduction band minimum (CBM) of the MAPI perovskite (−5.4 eV and −3.9 eV, respectively) and the methoxybenzene of arylamines moieties acts as good binding sites to the perovskite surface.[9] Still, **Spiro-OMeTAD** presents a series of fundamental flaws. It has intrinsic low hole mobility and low conductivity, and the addition of dopants (*e.g.* lithium bis(trifluoromethane)sulfonimide (Li-TFSI) and 4-*tert*-butylpyridine (*t*BP)) to improve such parameters not only is detrimental for the stability, reproducibility and device performances but also promotes undesired recombination phenomena.[3,10,11] None of the deposition methods of **Spiro-OMeTAD** on the perovskite layer proposed so far has delivered a completely optimal interfacial contact. Moreover, **Spiro-OMeTAD** does not represent an efficient barrier for the ionic migration from dopants, electrodes, and other PSC components.[12,13]

To overcome the drawbacks of **Spiro-OMeTAD**, a wide library of novel doped or dopant-free organic HTMs has been proposed and developed.[13,14] In particular, HTMs based on triphenylamines (TPA) and phenothiazine (PTZ) moieties (Scheme S1, ESI†) have attracted great research interest. The TPA moieties feature a non-planar geometry that confers unique hole transport properties, while the PTZ unit has an electron-donating butterfly structure, suitable for several kinds of functionalization, which allows the formation of stable radical cations.[14–26] HTMs designed from a combination of TPA and PTZ moieties, *e.g.* **PTZ2** reported by Grisorio *et al.*,[26] have shown efficiencies comparable to those obtained with **Spiro-OMeTAD**. With this aim, we recently designed *in silico* four novel TPA and PTZ-based HTMs, **HTM1-4**, and investigated their electronic properties by means of density functional theory (DFT) and time dependent density functional theory (TDDFT) methods; the results obtained for these novel HTMs were comparable to those obtained for **Spiro-OMeTAD** and **PTZ2**.[27] Among them, **HTM1** showed the highest occupied molecular orbital (HOMO) and the lowest unoccupied molecular orbital (LUMO) positions at −4.88 eV and −1.35 eV, respectively, hence higher in energy than the VBM and CBM of MAPI, respectively. Moreover, the wavefunction plot analysis revealed the HOMO of neutral **HTM1**, as well as the singly occupied molecular orbital (SOMO) of $(\mathbf{HTM1})^{\bullet+}$, are fully delocalized over the molecule, while the LUMO is confined on its central core. Such correct energy levels alignment and the slight HOMO LUMO overlap suggest that **HTM1** could possess good intermolecular hole-transport ability.[25] Moreover, the calculated absorption maximum of neutral **HTM1** was found to be 337 nm (3.68 eV), which minimizes competition with the perovskite absorption in the visible range, and it has shown good chemical hardness, higher than that of **Spiro-OMeTAD**.[27] Further synthesis and spectroscopic characterization ratified **HTM1** (also named **BPT-1**) as a valid HTM in PSCs.[28]

Although the design process of highly efficient PSCs largely benefits from physicochemical studies on isolated HTMs, it is also crucial to investigate their physicochemical interactions with the perovskite, as they strongly influence the ultimate performance of the devices.[13] Nevertheless, due to the large size of state-of-the-art HTMs, perovskite/organic HTM interfaces have been rarely studied from the computational point of view, and, thus, HTM adsorption features and interface electronic properties at the microscopic level are yet to be fully understood. To the best of our knowledge, the few computational studies available have explored the interfacial behavior of **Spiro-OMeTAD** on different MAPI surfaces.[29–32] The early work by Torres *et al.*[30] investigated the binding modes of methoxybenzene, *i.e.* **Spiro-OMeTAD** anchoring groups, on the MAPI (001) surface to clarify the HTM/perovskite attachment mechanism. They found that interaction mainly occurs when methoxy groups occupy MA^+ sites, while a repulsive behavior is observed with the surface iodine atoms.[30] Saliba *et al.*,[29] instead, theoretically investigated the whole **Spiro-OMeTAD**/MAPI interface. They focused on the interaction between the perovskite and the molecule and confirmed that it does not involve the core of the molecule but only the protruding methoxy groups.[29] The entire **Spiro-OMeTAD**/MAPI system has also been studied by Yin and co-workers.[31] This work points out the importance of the perovskite exposed facet in promoting the hole transfer. The most recent work devoted to a full **Spiro-OMeTAD**/MAPI interface by Wang *et al.*,[32] explores the role of interface termination, namely PbI_2 and MAI, in determining both the strength of the interaction with the MAPI (110) surface and the ability to ensure the charge transfer across the interface.[32] Besides the ones with **Spiro-OMeTAD**, other interfaces of the MAPI with TPA-based molecules have been theoretically investigated, both in terms of the interaction and driving force for the hole injection.[33–36] Motivated by the inspiring preliminary results obtained for isolated **HTM1**,[27] in this work we aim to assess the potential of the TPA and PTZ-based **HTM1** molecule as HTM in PSCs involving MAPI as an absorber by first-principles DFT-calculations. We first evaluate key electronic properties of isolated **HTM1** (Scheme 1(a)) related to the hole mobility and band alignment with the perovskite, such as the reorganization energies and redox potentials. In order to assess perovskite/HTM mutual polarization effects, we then investigate MAPI/**HTM1** interfaces, with **HTM1** in contact with either the PbI_2- or MAI-terminated MAPI (001) surface. Binding energies are

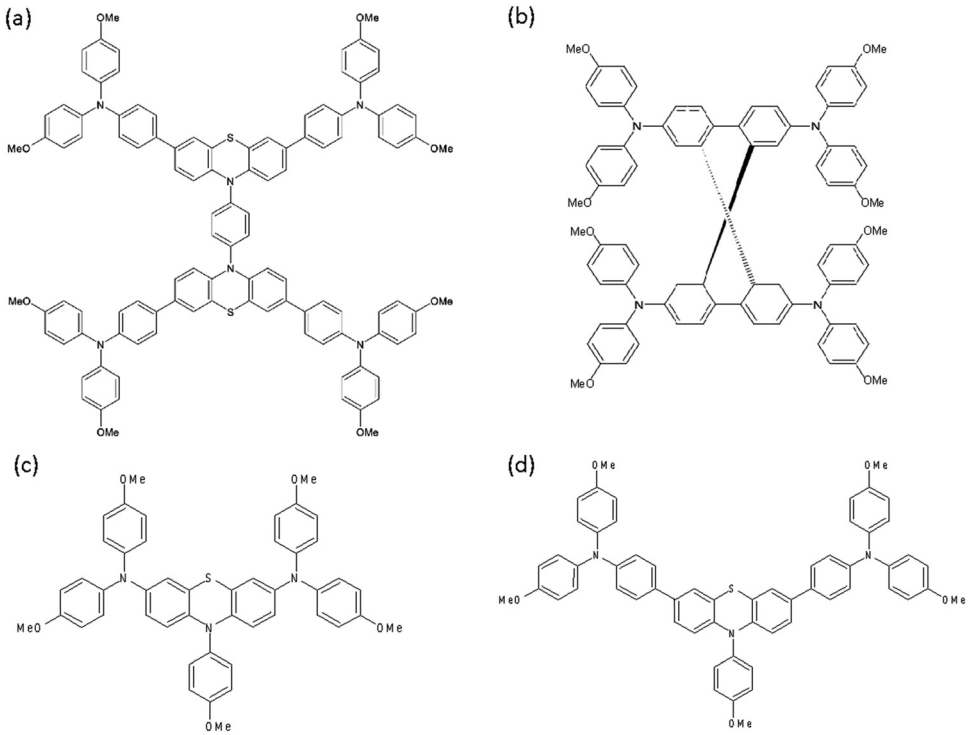

Scheme 1 Molecular structure drawings of molecules investigated in this work: (a) **HTM1** (b) **Spiro-OMeTAD** (c) **PTZ1** and (d) **PTZ2**.

rationalized in terms of structural modifications and bond formation, which are the main features leading to new channels for charge transport. We also assess how the mutual perovskite-**HTM1** polarization affects the HOMO-VBM alignment, providing results that contradict the results of isolated molecules, but allow us to understand available experimental outcomes, with direct implications on the final device performances. To allow a direct comparison with state-of-the-art and well-known TPA and PTZ-based HTMs, we extend our interfacial study to **Spiro-OMeTAD** (Scheme 1(b)), **PTZ1** (Scheme 1(c)) and **PTZ2** (Scheme 1(d)).[26]

Results and discussion

HTM molecular properties

The hole transport behaviour of HTMs is strongly influenced by the reorganization energy λ, *i.e.* the energy required to reorganize nuclei positions on a given oxidation state. The smaller the λ, the faster could be the hole transport,[37–39] indeed, the charge hopping rate (k) in our case can be defined by Marcus theory[40] as follows:

$$k = \frac{4\pi^2}{h} V^2 \frac{1}{\sqrt{4\pi\lambda k_B T}} \exp\left[-\frac{\lambda}{4k_B T}\right]$$

where h is the Planck's constant, V is the electronic coupling between adjacent molecules in the structure, λ is the reorganization energy, k_B is the Boltzmann constant and T is the temperature. The reported hopping rate is a special case of the more general Marcus formula that stands for the self-exchange reaction involving an electron exchange between two adjacent HTM molecules in which the free Gibbs energy change of the reaction is null. λ can be divided into inner-sphere reorganization energy (λ_{in}) and external reorganization energy (λ_{ext}). Considering that the latter accounts for the effect of the polarized medium on the charge transfer and that in organic solids is usually small, it is often neglected.[37,38] For this reason, only the contribution from the internal reorganization energy is considered here ($\lambda \cong \lambda_{in}$). Once the structures of the two electronic states involved in the hole transport event are known, λ can be obtained by the adiabatic potential energy surface method as follows:[37,38]

$$\lambda = \left(E_0^* - E_0\right) + \left(E_+^* - E_+\right)$$

where E_0^* represents the total energy of the neutral molecule at the cation geometry, E_0 is the total energy of the neutral molecule, E_+^* represents the total energy of the cation at the neutral molecule geometry and E_+ is the total energy of the cation. We must note that a full characterization of charge-transfer kinetic parameters (k, V) is beyond the purpose of this study, and it can be the object of future works. However, the comparison among the reorganization energies, which are intrinsic molecular properties, can provide insights into the different charge-transfer properties of these HTM molecules, as it has been already very helpful in rationalizing the behavior of different components in solar cells.[41–44] Inner-sphere reorganization energies of compounds **HTM1**, **Spiro-OMeTAD**, **PTZ1** and **PTZ2** computed in this way in vacuum are listed in Table 1.

The reorganization energy values present the trend **HTM1** < **Spiro-OMeTAD** < **PTZ2** < **PTZ1**, at both levels of theory, with the λ of **Spiro-OMeTAD** in accordance with the B3LYP results of Chi *et al.* in dichloromethane (0.131 eV).[45] This outcome

reports that the TPA and PTZ-based dimeric **HTM1** has a lower reorganization energy than those of the monomeric **PTZ1** and **PTZ2**. Additionally, it also has lower reorganization energy than that of **Spiro-OMeTAD**, hence we predicted good hole mobility and potentially minor need for further additive upon device assembly. The higher reorganization energies of **Spiro-OMeTAD**, **PTZ2** and **PTZ1** could be among the reasons behind the need for p-type doping, as reported in the literature.[26,46]

The low reorganization energy for **HTM1** can be associated with a slightly more rigid structure than those of the other molecules. Indeed, moving from its neutral to its oxidized form, we observed only a little average decrease of $\sim$0.01 Å along main bond lengths (C–C) and $\sim$3.1° in main dihedral angles (C–C–C–C) among the PTZ and the TPA moieties. Similarly, upon oxidation, the average bond lengths (C–N) and dihedral angles (C–C–N–C) among the 9,9′-spirobifluorene core and the arylamine moieties in **Spiro-OMeTAD** decreased by $\sim$0.01 Å and $\sim$4.6°, respectively. On the other hand, the decrease in the main bond lengths and dihedral angles among the PTZ and the TPA moieties is $\sim$0.2 Å (C–C) and $\sim$7° (C–C–C–C) moving from neutral to oxidized **PTZ2** and of $\sim$0.2 Å (C–N) and $\sim$12.7° (C–C–N–C) moving from neutral to oxidized **PTZ1**. Hence, by a difference of *ca.* 3.9°, in **PTZ2** the torsional freedom of the C–C–C–C dihedral angles among the PTZ and the TPA moieties is higher than that observed for **HTM1**, while the C–C–N–C dihedral angles of **PTZ1** have a torsional freedom higher than that of **PTZ2** of *ca* 5.7°. These increased values correspond to higher reorganization energy values with respect to those of **HTM1**.

Oxidation potentials (G_{ox}) have been calculated as the difference between the free energies of the neutral and the oxidized states of each molecule (G^0 and G^+, respectively), *i.e.* $G_{ox} = G^0 - G^+$, and are listed in Table 1. The computed G_{ox} values follow the expected trend for both DFT functionals. Indeed, a recent article by Wang *et al.*[47] reports oxidation potentials of 50 compounds, theoretically determined employing different exchange correlation functionals and compared with experimental values: pure functionals as PBE underestimate G_{ox}, while the presence of Hartree–Fock-like exchange in hybrid functionals increases the G_{ox} values.[47] In particular, the calculated G_{ox} for **Spiro-OMeTAD** with B3LYP/6-31G(d,p) in this work (−5.00 eV) is in good agreement with the one reported by Wang *et al.* at B3LYP/6-31G* (−4.98 eV) and with **Spiro-OMeTAD** experimental oxidation potential in CH_2Cl_2 (-5.09 eV).[32] Calculated G_{ox} of **PTZ1** (-4.95 eV) and **PTZ2** (-5.10 eV) are in fair agreement with the experimental oxidation potentials obtained at −4.77 eV and −5.15 eV by Grisorio *et al.*,[26] respectively. All lying in a narrow range, the G_{ox} of **HTM1** calculated and reported here for the first time is very similar to those of the other three analysed HTMs and it is higher in energy than the experimental value of the MAPI VBM potential ($\sim$−5.4 eV).[9,38]

Table 1 Inner-sphere reorganization energies (λ) and oxidation potentials (G_{ox}) of **HTM1**, **Spiro-OMeTAD**, **PTZ1** and **PTZ2**. All quantities are calculated in vacuum at both PBE/6-31G(d,p) and B3LYP/6-31G(d,p) levels of theory

MOLECULE	METHODS	λ (eV)	G_{ox} (eV)
HTM1	PBE/6-31G(d,p)	0.064	−4.48
	B3LYP/6-31G(d,p)	0.092	−4.99
Spiro-OMeTAD	PBE/6-31G(d,p)	0.087	−4.61
	B3LYP/6-31G(d,p)	0.132	−5.00
PTZ1	PBE/6-31G(d,p)	0.233	−4.66
	B3LYP/6-31G(d,p)	0.381	−4.95
PTZ2	PBE/6-31G(d,p)	0.139	−4.71
	B3LYP/6-31G(d,p)	0.217	−5.10

HTMs/MAPI interfaces: structures and energetics

MAPI features temperature-dependent structural phases: cubic, stable at high temperatures ($T > 330$ K), tetragonal at $160 < T < 330$ K and orthorhombic at low temperatures ($T < 160$ K).[48] By single-crystal X-ray diffraction analysis, the cubic structure (belonging to the *Pm*3*m* group) has been reported to be the most stable under operating conditions,[49] hence it has been adopted here to model MAPI interactions with **HTM1**, **Spiro-OMeTAD**, **PTZ1**, and **PTZ2**. The theoretically determined lattice constant for the MAPI bulk unit cell (Fig. S1(a), ESI†) at the PBE level, a = 6.256 Å, results in very good agreement with the experimental one (a = 6.276 Å).[49] From this bulk, two symmetric (non-stochiometric) five-layer slabs of the MAPI (001) surface have been constructed in order to simulate the two possible MAPI terminations, *i.e.*, PbI_2- and MAI-exposing facets, here identified as MAPI:PbI_2 (Fig. S1(b), ESI†) and MAPI:MAI (Fig. S1(c), ESI†). Among all surfaces, the (001) termination has been chosen since it has been reported as one of the most stable surfaces of the MAPI cubic and tetragonal phases.[30,35] The slabs composed of 5 crystal planes perpendicular to the c axis (plus a vacuum slab of 12 Å) are a good compromise between accuracy and computational costs from a surface energy convergence test made on 5, 7 and 9 crystal planes slabs (see the Slab convergence tests section in the ESI†).

A slab supercell with different periodicity within the xy plane has been considered for each termination and each HTM, according to their size, *i.e.* 7 × 7 for **HTM1**, 4 × 4 for **Spiro-OMeTAD** and **PTZ1** and 6 × 6 for **PTZ2**. In order to account for the molecule's complex structure and to obtain reliable energy minima for each termination, different adsorption modes of **HTM1** have been considered. **HTM1** has been placed on the MAPI surface either exposing the PTZ or the TPA moieties, which have been labeled as down and up orientations, respectively (Fig. S2, ESI†). The same strategy and labeling have been adopted also for **PTZ1** and **PTZ2** (Fig. S3 and S4, respectively, ESI†). In the case of **Spiro-OMeTAD**, it has been previously reported that it interacts with the MAPI surface exposing the methoxybenzene of the arylamine moieties,[29–32] thus the up and down orientations refer to the methoxybenzene of the two different facets of the 9,9′-spirobifluorene core. The minimum-energy interfaces from preliminary rigid scans have been allowed to relax without symmetry constraints. After relaxation, HTMs/MAPI:PbI_2 and HTMs/MAPI:MAI interface binding energies have been computed as follows:

$$E_{bind} = E_{interface} - E_{MAPI} - E_{molecule}$$

where $E_{interface}$ is the energy of the HTMs/MAPI system, E_{MAPI} is the energy of the isolated MAPI slabs and $E_{molecule}$ is the energy of the isolated HTMs. All the minimum-energy interfaces and their relative binding energies are shown in Fig. S2–S5 (ESI†), while the most stable interfaces of the considered HTMs/MAPI:PbI_2 and HTMs/MAPI:MAI systems are shown in Fig. 1 and 2, respectively, together with their binding energies. In particular, the most stable configurations of **HTM1**/MAPI, **PTZ1**/MAPI and **Spiro-OMeTAD**/MAPI have binding energies in the −1.49/−2.83 eV range for MAPI:PbI_2 and −2.14/−5.01 eV range for MAPI:MAI. On the other hand, the preferred **PTZ2**/MAPI interfaces are the most stable with a binding energy of −7.30 eV in the case of MAPI:PbI_2 and −6.08 eV for MAPI:MAI.

HTM1 preferably adopts the up orientation on both PbI_2 and MAI terminations, which causes some distortions in the overall surfaces (Fig. 1(a) and 2(a)) due to the interaction of methoxybenzene of the TPA moieties with the MAPI. In particular, **HTM1**/MAPI:MAI interaction is stronger than that calculated for **HTM1**/MAPI:PbI_2, due to the formation of some hydrogen bonds between the oxygen atoms of **HTM1** methoxybenzene groups and the hydrogen atoms of MAPI methylammonium cations. Differently, when **HTM1** adopts the down orientation on both MAPI:PbI_2 and MAPI:MAI, the resultant interaction with the MAPI (001) surface is just a localized event, which is initiated by the sulfur atoms of the PTZ moieties (Fig. S2, ESI†).

Despite the molecular similarities between **HTM1** and **PTZ2**, the latter gets stabilized by adopting the down orientation on both MAPI (001) terminations (Fig. 1(b) and 2(b)). In these cases, **PTZ2** interacts with MAPI by exposing the sulfur atom of the PTZ moiety and additional interactions occur through the methoxybenzene of the TPA moieties and from the methoxybenzene directly linked to the PTZ nitrogen. These additional interactions are unlikely to occur in **HTM1**, since the benzene ring linking the two PTZ moieties has limited rotational freedom and the molecule is overall more rigid, which limits the interactions between the TPA moieties and the MAPI in the down orientation (Fig. S6, ESI†). Regarding **PTZ1**/MAPI, the up orientations are preferred, where the HTM exposes the metoxybenzene of arylamine moieties. More convenient binding energies for **PTZ1**/MAPI:MAI than for **PTZ1**/MAPI:PbI_2 can be attributed to the formation of hydrogen bonds between the oxygen of methoxybenzene and the hydrogens of methylammonium cations (Fig. 1(c) and 2(c)), as it also occurs for **HTM1**/MAPI:MAI (up). Indeed, differently from **PTZ2**, when **PTZ1** adopts the down orientation, the sulfur atom of the PTZ moiety is less involved in the interaction with MAPI, because of a more pronounced torsion of the methoxybenzene directly linked to the PTZ nitrogen, which has an almost parallel position during the interaction in **PTZ2** instead (Fig. S7, ESI†). As for **Spiro-OMeTAD**, our calculations are in close agreement with previous results[29–32] reporting the down orientation as the preferred one on MAPI surfaces (Fig. 1(d) and 2(d)). **Spiro-OMeTAD**, indeed, interacts with the MAPI through the methoxybenzene of arylamine moieties. In particular, when **Spiro-OMeTAD** adopts the down orientation, methoxybenzene has a preferential arrangement with respect to the MAPI surface, which allows a closer interaction between the molecule and the surface, thus contributing to stabilizing the binding energy values. Hence, in the case of **Spiro-OMeTAD**/MAPI:PbI_2 the oxygens of methoxybenzene interact with the Pb atoms of the MAPI (Fig. 1(d)), while in the case of **Spiro-OMeTAD**/MAPI:MAI the oxygens of methoxybenzene interact with the hydrogens of methylammonium cations (Fig. 2(d)). While in the first case the interaction is stronger than those of **HTM1**/MAPI:PbI_2 and **PTZ1**/MAPI:PbI_2, **Spiro-OMeTAD**/MAPI:MAI has lower binding energy with respect to **HTM1**/MAPI:MAI and **PTZ1**/MAPI:MAI, which are more stabilized thanks to the formation of hydrogen bonds between the molecules and the MAPI surface. Indeed, while in **HTM1**/MAPI:MAI and **PTZ1**/MAPI:MAI the distances among the oxygen atoms of the methoxybenzene and some hydrogen atoms of the methylammonium cations recall the typical distances of an intermolecular hydrogen bond (*e.g.*

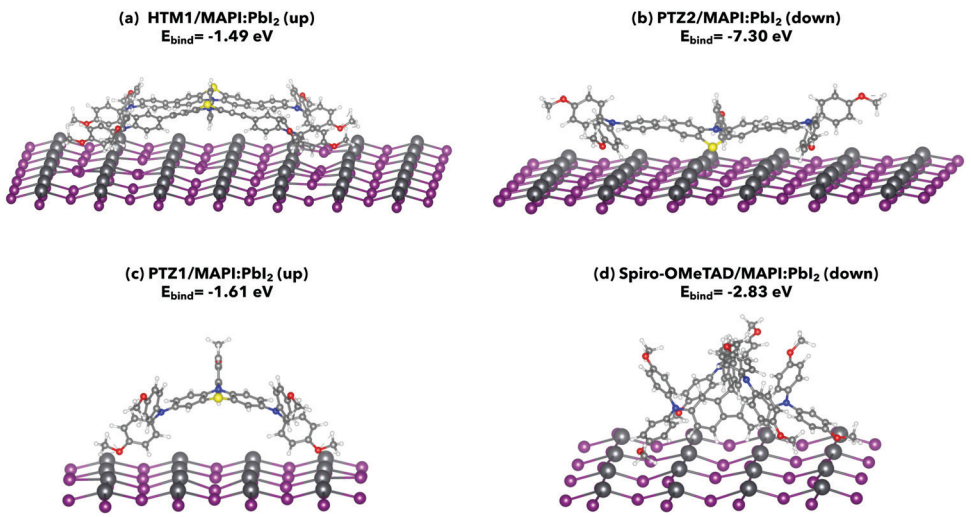

Fig. 1 Most stable interfaces and corresponding binding energies (E_{bind}) of (a): **HTM1**/MAPI:PbI_2, (b) **PTZ2**/MAPI:PbI_2, (c) **PTZ1**/MAPI:PbI_2, and (d) **Spiro-OMeTAD**/MAPI:PbI_2 systems. Color code: Pb-dark gray; I-violet; C-light grey; N-blue; H-white; O-red; S-yellow.

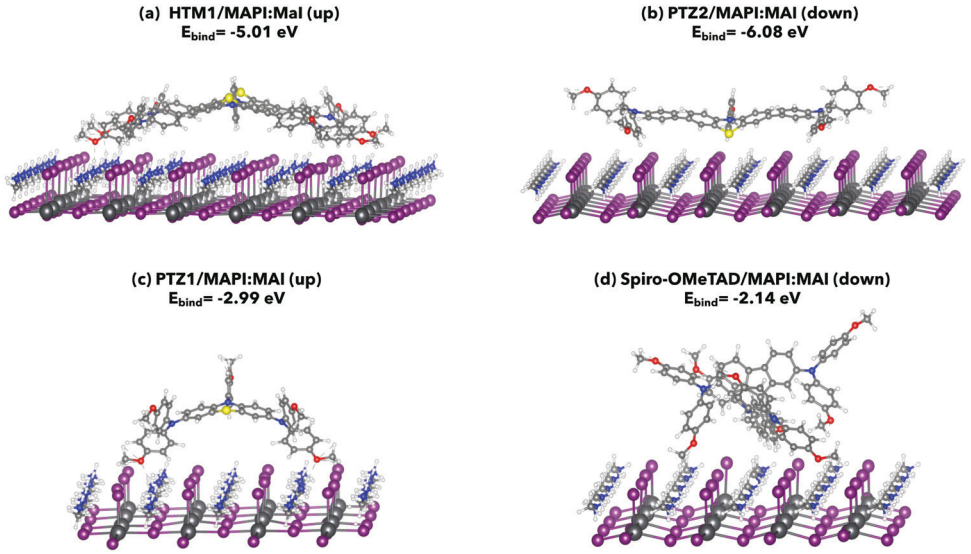

Fig. 2 Most stable interfaces and corresponding binding energies (E_{bind}) of (a): **HTM1**/MAPI:MAI, (b) **PTZ2**/MAPI:MAI, (c) **PTZ1**/MAPI:MAI, and (d) **Spiro-OMeTAD**/MAPI:MAI. Color code: Pb-dark gray; I-violet; C-light grey; N-blue; H-white; O-red; S-yellow.

dO_7–H_{828} = 1.74 Å in **HTM1**/MAPI, dO_1–H_{275} = 1.73Å in **PTZ1**/MAPI), major distances are found in **Spiro-OMeTAD**/MAPI (*e.g.* dO_2–H_{143} = 2.17 Å).

HTMs/MAPI interfaces: electronic features

The electronic properties of the investigated HTMs/MAPI systems have also been analyzed in terms of their projected density of states (pDOS). The pDOS plots of the most stable interfaces of HTMs/MAPI:PbI_2 and HTMs/MAPI:MAI systems are depicted in Fig. 3 and 4, respectively. Close-up views near the Fermi level are reported in Fig. S8 and S9 (ESI†).

Regarding PbI_2-terminated surfaces (Fig. 3), the pDOS reveal that the VBM of MAPI slightly lies at a higher energy than the HOMO level of **HTM1** and **PTZ2** (Fig. 3(a and b)). Thus for the standard MAPI perovskite, there is no adequate driving force for the hole-injection process and undesired charge-recombination events can occur. Differently, in the cases of **Spiro-OMeTAD** and **PTZ1**, the pDOS highlight a slight but convenient driving force for the hole injection at the MAPI:PbI_2 interfaces (see also the zoom-in of the pDOS in Fig. S8 in the ESI†). Indeed, the HOMO levels of **Spiro-OMeTAD** and **PTZ1** are slightly higher in energy than the MAPI VB edge, thus granting

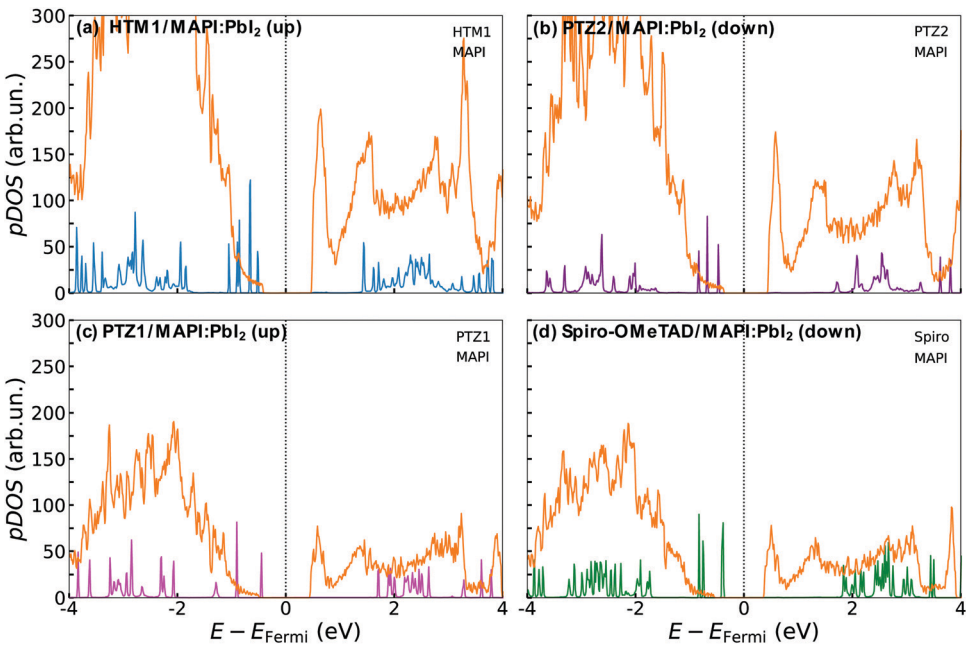

Fig. 3 pDOS plots of (a) **HTM1**/MAPI:PbI_2 (up), (b) **PTZ2**/MAPI:PbI_2 (down), (c) **PTZ1**/MAPI:PbI_2 (up) and (d) **Spiro-OMeTAD**/MAPI:PbI_2 (down), computed at GGA-PBE, including D3BJ dispersion forces.

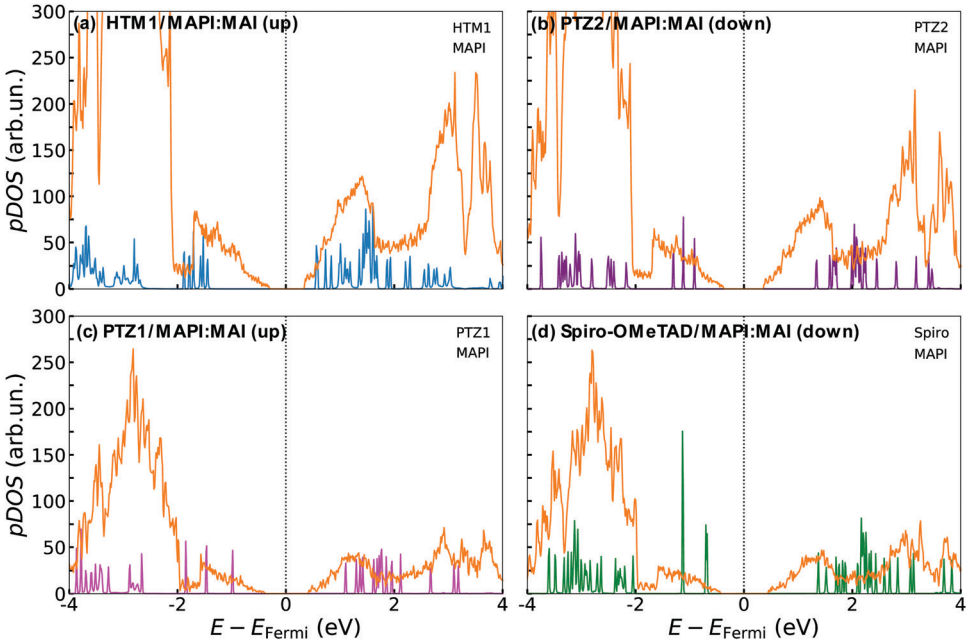

Fig. 4 pDOS plots of (a) **HTM1**/MAPI:MAI (up), (b) **PTZ2**/MAPI:MAI (down), (c) **PTZ1**/MAPI:MAI (up) and (d) **Spiro-OMeTAD**/MAPI:MAI (down) computed at GGA-PBE, including D3BJ dispersion forces.

a convenient extraction of the hole from the photo-excited MAPI.

As for HTMs/MAPI:MAI interfaces (Fig. 4), the VBM of MAPI is higher in energy than the HOMO levels of all HTMs considered. Thus, these interfaces, although energetically very stable, do not provide a sufficient driving force for the holes to be injected into the HTMs.

Considering these results, the prototypical MAPI perovskite has resulted in an inefficient charge transport process when combined with TPA and PTZ-based molecules. For this reason, if it is to be adopted for the construction of PSC devices, the chemical doping of **HTM1** could be considered as a valid approach to increase its HOMO energy level. Still, since isolated **HTM1** possesses optimal properties to be used as a dopant-free HTM and it is well known that the doping could lead to perovskite degradation,[3,4,9,13–15] an alternative and valid strategy could consist in the exploration of different kinds of perovskite compositions to understand the potential of this molecule in PSC devices. As a matter of fact, the properties of dopant-free **HTM1** (also named **BPT-1**) have been recently investigated in a methylammonium-free p–i–n PSC, adopting $Cs_{0.17}FA_{0.83}Pb(I_{0.9}Br_{0.1})_3$ as the perovskite and achieving 17.26% PCE, while that obtained employing the standard PTAA in the same experimental conditions is found to be 17.96%.[28] This result further corroborates the suitability of **HTM1** as HTM, as well as the influence of the perovskite formulation on the hole transport process. Additionally, the promising performances of PSC devices built with **PTZ2** as HTM have been reported together with the use of dopants but most of all considering the employment of the mixed halide (bromine and iodine) and cations (methylammonium, formamidinium and cesium) perovskite.[26] Hence, this is an additional proof that the interaction between the HTMs and the perovskite is not the only parameter influencing the charge transport process. Indeed, a good binding motif does not always provide sufficient driving force for the hole injection/extraction, but also the perovskite composition plays a fundamental role in determining an effective charge transport process.

Conclusions

In this work, DFT methods have been employed to study the electronic properties of a novel triphenylamine and phenothiazine-based molecule, **HTM1**, in its isolated form and when it interacts with the MAPI (001), considering the two possible MAPI terminations, PbI_2 and MAI. The results have been compared with those obtained for well-known hole transport materials already present in the literature, such as **Spiro-OMeTAD**, **PTZ1**, and **PTZ2**, to investigate the potential applicability of **HTM1** in MAPI-based perovskite solar cells, and to provide new insights into the hole transport behavior at the interface between MAPI and TPA and PTZ-based molecules.

The calculations revealed that **HTM1** has the lowest reorganization energy, hence it could possess good hole mobility, while its G_{ox} is well aligned with those of **Spiro-OMeTAD**, **PTZ1**, and **PTZ2**, which would allow its application as HTM in common PSCs. The investigation of the structural and electronic properties of **HTM1**/MAPI has shown that **HTM1** has a good interaction with both MAPI:PbI_2 and MAPI:MAI, when it exposes the methoxybenzene of TPA moieties. In particular, the interaction with MAPI:MAI results in a more stabilized binding energy, due to the formation of hydrogen bonds between the oxygen atoms of methoxybenzene and the hydrogen atoms of

methylammonium cations. Nevertheless, from the pDOS plots it has been found that the HOMO level of **HTM1** has lower energy than the VBM of MAPI, thus we found that sufficient driving force is not available for the hole injection process to occur. An inadequate driving force for the hole injection/extraction has also been found for **PTZ2**/MAPI, even if the latter presents the most stabilized binding energies thanks to the presence of additional interactions. In the end, **Spiro-OMeTAD** and **PTZ1** have shown a convenient but low driving force for the hole extraction from the MAPI:PbI_2 configuration. Hence, from this study, it emerged that the intrinsic HTM properties and the binding motif are not the only parameters influencing the charge transport process, while the perovskite composition can also strongly affect it. Besides MAPI perovskite is often taken as a reference for the investigation of electronic properties at the interface with HTMs, it has resulted to be inadequate for TPA and PTZ-based molecules. This finding supports the limited employment of MAPI for the real fabrication of devices. For this reason and to shed further light on interfacial processes, additional computational studies involving a different kind of perovskite composition should be performed. Moreover, more TPA and PTZ-based HTM conformations on MAPI surface could be explored to further analyze the dynamics of the charge transport processes.

Methods and computational details

Geometry optimizations of neutral and oxidized **HTM1**, **Spiro-OMeTAD**, **PTZ1** and **PTZ2** have been performed *via* density functional theory (DFT)[50,51] at the B3LYP/6-31G(d,p)[52,53] and PBE/6-31G(d,p)[54,55] levels of theory *in vacuo*, using Gaussian 16, Revision C.01 suite of programs.[56] Dispersion forces have been included within the Grimme's D3 framework[57] using the damping scheme by Becke and Johnson (D3BJ).[58,59] Frequency calculations have been performed to check that stationary points were true energy minima.

HTMs reorganization energies *in vacuo* of compounds **HTM1**, **Spiro-OMeTAD**, **PTZ1** and **PTZ2** have been calculated at the PBE/6-31G(d,p) and B3LYP/6-31G(d,p) levels of theory, on the lowest energy neutral and oxidized geometries optimized at the PBE/6-31G(d,p) and B3LYP/6-31G(d,p) levels of theory, respectively.

To investigate HTMs/MAPI structural and electronic properties, the cubic structure of the MAPI bulk and the four considered compounds have been optimized with Periodic Boundary Conditions (PBC) *via* DFT at PBE-GGA, using the DZP basis set, including $5d^{10}$ semicore electrons for Pb atoms,[60] along with Troullier–Martins norm-conserving pseudopotentials,[61,62] as implemented in the SIESTA 4.1 program package.[63] A mesh cutoff of 400 Ry and $8 \times 8 \times 8$ and $1 \times 1 \times 1$ Γ-centered Monkhorst–Pack *k*-point grid for sampling the Brillouin zone have been considered respectively for the optimization of the MAPI bulk and for the optimization of **HTM1**, **Spiro-OMeTAD**, **PTZ1** and **PTZ2**.

In the same way, the HTMs/MAPI energy minima have been optimized at PBE-GGA, using the DZP basis set, including $5d^{10}$ semicore electrons for Pb atoms, along with Troullier–Martins norm-conserving pseudopotentials. A mesh cutoff of 400 Ry and a $1 \times 1 \times 1$ Γ-centered Monkhorst–Pack *k*-point grid have been considered. SCF energy threshold and total force threshold have been set at 10^{-5} eV and 0.01 eV $Å^{-1}$, respectively, for each geometry optimization. The binding energies have been determined through single point calculations on the optimized systems at $8 \times 8 \times 1$ Γ-centered Monkhorst–Pack *k*-point grid. The energies of all investigated systems have been corrected including the dispersion force calculated by the D3BJ damping scheme. We must note that more accurate quantitative predictions of the electronic properties would require a perturbative approach (*e.g.* GW) and inclusion of the spin orbit coupling (SOC) effects, which influence both the optical and electronic properties of compounds involving heavy atoms such as Pb. However, such an approach is more computationally expensive than DFT and would not be feasible for our interface systems. On the other hand, the combination of DFT+SOC predicts bandgaps very different from experiments. In particular, SOC addition affects to a larger extent the conduction band (made of Pb, p states) while retaining the position of the iodine (p) states forming the valence band. This results in a strong underestimation of the experimental bandgap.[11] Moreover, we expect that the SOC would equally affect all the considered interfaces, so neglecting it in all calculations does not prevent us to make a qualitative comparison of the different HTMs, that is the purpose of this work.

Conflicts of interest

There are no conflicts to declare.

Acknowledgements

The computing resources and the related technical support used for this work have been provided by the CRESCO/ENEAGRID High Performance Computing Infrastructure and its staff.[64] CRESCO/ENEAGRID High Performance Computing Infrastructure is funded by ENEA, the Italian National Agency for New Technologies, Energy and Sustainable Economic Development and by Italian and European research programmes, see **https://www.cresco.enea.it/english** for information. C. C. and A. S. also acknowledge the Department of Biotechnology, Chemistry and Pharmacy, Department of Excellence 2018–2022 and the hpc@dbcf for providing computational resources.

References

1 J. Jeong, M. Kim, J. Seo, H. Lu, P. Ahlawat, A. Mishra, Y. Yang, M. A. Hope, F. T. Eickemeyer, M. Kim, Y. J. Yoon, I. W. Choi, B. P. Darwich, S. J. Choi, Y. Jo, J. H. Lee, B. Walker, S. M. Zakeeruddin, L. Emsley, U. Rothlisberger, A. Hagfeldt, D. S. Kim, M. Grätzel and J. Y. Kim, *Nature*, 2021, **592**, 381–385.

2 NREL. Best Research-Cell Efficiency Chart, https://www.nrel.gov/pv/cell-efficiency.html, (Accessed November 2021).
3 J. Y. Kim, J.-W. Lee, H. S. Jung, H. Shin and N.-G. Park, *Chem. Rev.*, 2020, **120**, 7867–7918.
4 S. A. Olaleru, J. K. Kirui, D. Wamwangi, K. T. Roro and B. Mwakikunga, *Sol. Energy*, 2020, **196**, 295–309.
5 D. Zhou, T. Zhou, Y. Tian, X. Zhu and Y. Tu, *J. Nanomater.*, 2018, **2018**, 8148072.
6 L. A. Castriotta, R. F. Pineda, V. Babu, P. Spinelli, B. Taheri, F. Matteocci, F. Brunetti, K. Wojciechowski and A. Di Carlo, *ACS Appl. Mater. Interfaces*, 2021, **13**, 29576–29584.
7 M. Vasilopoulou, A. Fakharuddin, A. G. Coutsolelos, P. Falaras, P. Argitis, A. R.-B. M. Yusoffd and M. K. Nazeeruddin, *Chem. Soc. Rev.*, 2020, **49**, 4496–4526.
8 R. Singh, P. K. Singh, B. Bhattacharya and H.-W. Rhee, *Appl. Mater. Today*, 2019, **14**, 175–200.
9 J. Urieta-Mora, I. García-Benito, A. Molina-Ontoria and N. Martín, *Chem. Soc. Rev.*, 2018, **47**, 8541–8571.
10 G. Ren, W. Han, Y. Deng, W. Wu, Z. Li, J. Guo, H. Bao, C. Liu and W. Guo, *J. Mater. Chem. A*, 2021, **9**, 4589–4625.
11 A. Pecoraro, A. De Maria, P. Delli Veneri, M. Pavone and A. B. Muñoz-García, *Phys. Chem. Chem. Phys.*, 2020, **22**, 28401–28413.
12 H. Taherianfard, G.-W. Kim, F. Ebadi, T. Abzieher, K. Choi, U. W. Paetzold, B. S. Richards, A. A. Eliwi, F. Tajabadi, N. Taghavinia and M. M. Byranvand, *ACS Appl. Mater. Interfaces*, 2019, **11**, 44802–44810.
13 F. M. Rombach, S. A. Haque and T. J. Macdonald, *Energy Environ. Sci.*, 2021, **14**, 5161–5190.
14 H. D. Pham, T. C. J. Yang, S. M. Jain, G. J. Wilson and P. Sonar, *Adv. Energy Mater.*, 2020, **10**, 1903326.
15 E. Sheibani, L. Yang and J. Zhang, *Sol. RRL.*, 2020, **4**, 1–16.
16 R. Hussain, M. Y. Mehboob, M. U. Khan, M. Khalid, Z. Irshad, R. Fatima, A. Anwar, S. Nawab and M. Adnan, *J. Mater. Sci.*, 2021, **56**, 5113–5131.
17 M. Li, S. Ma, M. Mateen, X. Liu, Y. Ding, J. Gao, Y. Yang, X. Zhang, Y. Wu and S. Dai, *Sol. Energy*, 2020, **195**, 618–625.
18 M. R.-S. A. Janjua, *Chem. – Eur. J.*, 2021, **27**, 4197–4210.
19 S. A. Siddique, M. B. A. Siddique, R. Hussain, X. Liu, M. Y. Mehboob, Z. Irshad and M. Adnan, *Comput. Theor. Chem.*, 2020, **1191**, 113045.
20 X. Liu, X. Tan, Q. Chen, H. Shan, C. Liu, J. Xu, Z. K. Chen, W. Huang and Z. X. Xu, *RSC Adv.*, 2017, **7**, 53604–53610.
21 C. Lu, M. Paramasivam, K. Park, C. H. Kim and H. K. Kim, *ACS Appl. Mater. Interfaces*, 2019, **11**, 14011–14022.
22 S. Revoju, A. Matuhina, L. Canil, H. Salonen, A. Hiltunen, A. Abate and P. Vivo, *J. Mater. Chem. C*, 2020, **8**, 15486–15506.
23 J. Salunke, X. Guo, M. Liu, Z. Lin, N. R. Candeias, A. Priimagi, J. Chang and P. Vivo, *ACS Omega*, 2020, **5**, 23334–23342.
24 S. Thokala and S. P. Singh, *ACS Omega*, 2020, **5**, 5608–5619.
25 F. Zhang, S. Wang, H. Zhu, X. Liu, H. Liu, X. Li, Y. Xiao, S. M. Zakeeruddin and M. Grätzel, *ACS Energy Lett.*, 2018, **3**, 1145–1152.
26 R. Grisorio, B. Roose, S. Colella, A. Listorti, G. P. Suranna and A. Abate, *ACS Energy Lett.*, 2017, **2**, 1029–1034.
27 C. Coppola, R. Infantino, A. Dessì, L. Zani, M. L. Parisi, A. Mordini, G. Reginato, R. Basosi and A. Sinicropi, *Mater. Chem. Phys.*, 2022, **278**, 125603.
28 L. A. Castriotta, R. Infantino, L. Vesce, M. Stefanelli, A. Dessì, C. Coppola, M. Calamante, G. Reginato, A. Mordini, A. Sinicropi, A. Di Carlo and L. Zani, submitted manuscript.
29 M. Saliba, S. Orlandi, T. Matsui, S. Aghazada, M. Cavazzini, J.-P. Correa-Baena, P. Gao, R. Scopelliti, E. Mosconi, K.-H. Dahmen, F. De Angelis, A. Abate, A. Hagfeldt, G. Pozzi, M. Graetzel and M. K. Nazeeruddin, *Nat. Energy*, 2016, **1**, 15017.
30 A. Torres and L. G.-C. Rego, *J. Phys. Chem. C*, 2014, **118**, 26947–26954.
31 J. Yin, D. Cortecchia, A. Krishna, S. Chen, N. Mathews, A. C. Grimsdale and C. Soc, *J. Phys. Chem. Lett.*, 2015, **6**, 1396–1402.
32 Q. Wang, E. Mosconi, C. Wolff, J. Li, D. Neher, F. De Angelis, G. P. Suranna, R. Grisorio and A. Abate, *Adv. Energy Mater.*, 2019, **9**, 1900990.
33 Y. Zhang, P. Heng, H. Su, J. Li, J. Guo, P. Ning, W. Wu, T. Ren, L. Wang and J. Zhang, *Chem. Rec.*, 2018, **18**, 1–10.
34 Y. Zhang, J. Guo, H. Su, J. Li, W. Wu and L. Wang, *Dyes Pigm.*, 2018, **154**, 275–281.
35 Y. Li, Y. Zhang, J. Zhang, J. Li, W. Wu and L. Wang, *Org. Electron.*, 2018, **62**, 591–597.
36 Y. Li, Y. Zhang, P. Heng, R. Shao, Y. Liu, W. Qiao, L. Wanga and J. Zhang, *Org. Electron.*, 2018, **54**, 14–20.
37 Z. Zhang and R. He, *Comput. Theor. Chem.*, 2019, **1161**, 10–17.
38 J. Deng, W. Hu, W. Shen, M. Li and R. He, *Phys. Chem. Chem. Phys.*, 2019, **21**, 1235–1241.
39 J. Simokaitiene, M. Cekaviciute, K. Baucyte, D. Volyniuk, R. Durgaryan, D. Molina, B. Yang, J. Suo, Y. J. Kim, D. A. da Silva Filho, A. Hagfeldt, G. Sini and J. V. Grazulevicius, *ACS Appl. Mater. Interfaces*, 2021, **13**, 21320–21330.
40 R. A. Marcus, *Rev. Mod. Phys.*, 1993, **65**, 599–610.
41 Y. Saygili, M. Söderberg, N. Pellet, F. Giordano, Y. Cao, A. B. Muñoz-García, S. M. Zakeeruddin, N. Vlachopoulos, M. Pavone, G. Boschloo, L. Kavan, J.-E. Moser, M. Grätzel, A. Hagfeldt and M. Freitag, *J. Am. Chem. Soc.*, 2016, **138**, 15087–15096.
42 Y. Saygili, M. Stojanovic, H. Michaels, J. Tiepelt, J. Teuscher, A. Massaro, M. Pavone, F. Giordano, S. M. Zakeeruddin, G. Boschloo, J.-E. Moser, M. Grätzel, A. B. Muñoz-García, A. Hagfeldt and M. Freitag, *ACS Appl. Energy Mater.*, 2018, **1**, 4950–4962.
43 Y. Saygili, M. Stojanovic, N. Flores-Díaz, S. M. Zakeeruddin, N. Vlachopoulos, M. Grätzel and A. Hagfeldt, *Inorganics*, 2018, **7**, 30.
44 A. B. Muñoz-García, I. Benesperi, G. Boschloo, J. J. Concepcion, J. H. Delcamp, E. A. Gibson, G. J. Meyer, M. Pavone, H. Pettersson, A. Hagfeldt and M. Freitag, *Chem. Soc. Rev.*, 2021, **50**, 12450–12550.
45 W.-J. Chi, Q.-S. Li and Z.-S. Li, *Nanoscale*, 2016, **8**, 6146–6154.
46 Y. Li, H. Li, C. Zhong, G. Sini and J.-L. Brédas, *npj Flex Electron*, 2017, **1**, 1–8.

47 D. Wang, S. Huang, C. Wang, Y. Yue and Q. Zhang, *Org. Electron.*, 2019, **64**, 216–222.
48 C. T. Crespo, *J. Phys. Chem. Solids*, 2021, **152**, 109958.
49 F. F. Targhi, Y. S. Jalili and F. Kanjouri, *Results Phys.*, 2018, **10**, 616–627.
50 P. Hohenberg and W. Kohn, *Phys. Rev.*, 1964, **136**, B864–B871.
51 W. Kohn and L. J. Sham, *Phys. Rev.*, 1965, **140**, A1134–A1138.
52 A. D. Becke, *J. Chem. Phys.*, 1993, **98**, 5648–5652.
53 C. Lee, W. Yang and R. G. Parr, *Phys. Rev. B: Condens. Matter Mater. Phys.*, 1988, **37**, 785–789.
54 J. P. Perdew, K. Burke and M. Ernzerhof, *Phys. Rev. Lett.*, 1996, **77**, 3865–3868.
55 J. P. Perdew, K. Burke and M. Ernzerhof, *Phys. Rev. Lett.*, 1997, **78**, 1396.
56 M. J. Frisch, G. W. Trucks, H. B. Schlegel, G. E. Scuseria, M. A. Robb, J. R. Cheeseman, G. Scalmani, V. Barone, G. A. Petersson, H. Nakatsuji, X. Li, M. Caricato, A. V. Marenich, J. Bloino, B. G. Janesko, R. Gomperts, B. Mennucci, H. P. Hratchian, J. V. Ortiz, A. F. Izmaylov, J. L. Sonnenberg, D. Williams-Young, F. Ding, F. Lipparini, F. Egidi, J. Goings, B. Peng, A. Petrone, T. Henderson, D. Ranasinghe, V. G. Zakrzewski, J. Gao, N. Rega, G. Zheng, W. Liang, M. Hada, M. Ehara, K. Toyota, R. Fukuda, J. Hasegawa, M. Ishida, T. Nakajima, Y. Honda, O. Kitao, H. Nakai, T. Vreven, K. Throssell, J. A. Montgomery, Jr., J. E. Peralta, F. Ogliaro, M. J. Bearpark, J. J. Heyd, E. N. Brothers, K. N. Kudin, V. N. Staroverov, T. A. Keith, R. Kobayashi, J. Normand, K. Raghavachari, A. P. Rendell, J. C. Burant, S. S. Iyengar, J. Tomasi, M. Cossi, J. M. Millam, M. Klene, C. Adamo, R. Cammi, J. W. Ochterski, R. L. Martin, K. Morokuma, O. Farkas, J. B. Foresman and D. J. Fox, *Gaussian 16 (Revision C.01)*, Gaussian, Inc., Wallingford CT, 2016.
57 S. Grimme, J. Antony, S. Ehrlic and S. Krieg, *J. Chem. Phys.*, 2010, **132**, 154104.
58 S. Grimme, S. Ehrlich and L. Goerigk, *J. Comput. Chem.*, 2011, **32**, 1456.
59 A. D. Becke and E. R.-J. Johnson, *Chem. Phys.*, 2005, **122**, 154101.
60 J. Junquera, Ó. Paz, D. Sánchez-Portal and E. Artacho, *Phys. Rev. B: Condens. Matter Mater. Phys.*, 2001, **64**, 235111.
61 N. Troullier and J. L. Martins, *Solid State Commun.*, 1990, **74**, 613–616.
62 N. Troullier and J. L. Martins, *Phys. Rev. B: Condens. Matter Mater. Phys.*, 1993, **43**, 1993–2006.
63 J. M. Soler, E. Artacho, J. D. Gale, A. García, J. Junquera, P. Ordejón and D. Sánchez-Portal, *J. Phys.: Condens. Matter*, 2002, **14**, 2745–2779.
64 F. Iannone, F. Ambrosino, G. Bracco, M. De Rosa, A. Funel, G. Guarnieri, S. Migliori, P. Palombi, G. Ponti, G. Santomauro and P. Procacci, *International Conference on High Performance Computing & Simulation (HPCS)*, Dublin, Ireland, 2019, pp. 1051–1052.